






JGR Solid Earth



RESEARCH ARTICLE

10.1029/2022JB026090

Influence of Viscous Lubricant on Nucleation and Propagation of Frictional Ruptures

F. Paglialunga¹ , F. Passelègue² , S. Latour³ , A. Gounon³ , and M. Violay¹ 

¹École Polytechnique Fédérale de Lausanne, Lausanne, Switzerland, ²Geoazur, Nice, France, ³Université Toulouse 3 - Paul Sabatier, Toulouse, France

Key Points:

- Frictional strength of lubricated artificial interfaces is dramatically reduced under mixed lubrication conditions
- Nucleation length of rupture under lubricated conditions is larger than the one of ruptures under dry conditions
- Viscous lubrication (under mixed conditions) can affect the nature of ruptures that would propagated pulse-like rather than crack-like

Correspondence to:

F. Paglialunga,
federica.paglialunga@epfl.ch

Citation:

Paglialunga, F., Passelègue, F., Latour, S., Gounon, A., & Violay, M. (2023). Influence of viscous lubricant on nucleation and propagation of frictional ruptures. *Journal of Geophysical Research: Solid Earth*, 128, e2022JB026090. <https://doi.org/10.1029/2022JB026090>

Received 21 NOV 2022

Accepted 25 MAR 2023

Author Contributions:

Conceptualization: F. Paglialunga, F. Passelègue, M. Violay

Data curation: F. Paglialunga, A. Gounon

Formal analysis: F. Paglialunga, F. Passelègue

Funding acquisition: S. Latour, M. Violay

Investigation: F. Paglialunga, F. Passelègue, S. Latour, A. Gounon

Resources: S. Latour

Supervision: M. Violay

Writing – original draft: F. Paglialunga

Writing – review & editing: F. Passelègue, S. Latour, M. Violay

Abstract Fluids are pervasive in the Earth's crust and saturate fractures and faults. The combination of fluids and gouge layers developing along faults can generate fluids of different viscosities. Such viscous fluids were found to influence the reactivation, frictional stability of faults, and eventually the dynamics of propagating earthquake ruptures. We reproduced laboratory earthquakes on analog material (PMMA) to study the influence of viscous lubricant on fault frictional stability, rupture nucleation, and propagation under mixed lubrication conditions. Experiments were conducted in dry conditions, and with fluids presenting a viscosity ranging from 1 to 1,000 mPa.s. Through photoelasticity, high-frequency strain gauge sensors, and accelerometer measurements, we obtained new insights about the influence of lubricant on a characteristic nucleation length, rupture propagation velocity, and local slip and slip rate evolution during the reproduced frictional ruptures. Our experiments show that the presence of a lubricant generating mixed lubricated conditions along the fault induces, (a) a reduction of the frictional resistance, (b) an increase in nucleation length, (c) a decrease in the fracture energy. In addition, the larger the viscosity of the fluids, the larger the reduction of frictional strength and the increase in the nucleation length. Moreover, ruptures occurring under mixed lubricated conditions showed a pulse-like rather than crack-like behavior, suggesting that viscous lubrication can induce the transition from crack-like to pulse-like rupture along natural faults. We demonstrate, supported by existing theory, that this transition is mainly governed by the stress acting on the fault at the onset of nucleation, which is drastically reduced in presence of a lubricant.

Plain Language Summary Fluids naturally permeating the Earth's crust or being injected for reservoir stimulation can promote fault reactivation, resulting in natural or so-called induced earthquakes. It is important to comprehend how the presence of these fluids, as well as their properties, affect the activation and magnitude of seismic events. In particular, we investigated the role of fluid viscosity under controlled experimental conditions through laboratory experiments on analog material. We show that for the same applied normal stress, faults under lubricated conditions (i.e., where a thin film of viscous lubricant had been spread) can be activated at much lower shear stresses than dry faults. At the same time, the generated events will be much smaller in magnitude (i.e., smaller stress drop) and propagate more stably.

1. Introduction

The presence of fluids in the upper Earth's crust is crucial to assess fault stability. The fluid overpressure decreases the effective normal stress acting on the fault plane, promoting fault reactivation (i.e., earthquakes; Leclère & Fabbri, 2013; Sibson, 1985a). Fault reactivation can also be favored by fluid injection during geo-reservoir stimulations and is accompanied by small magnitude (sometimes larger; human) induced earthquakes (Ellsworth, 2013; Majer et al., 2007).

To better comprehend the physical mechanisms that occur on fault during the increase of the fluid pressure, numerous works studied fault reactivation in the laboratory, based on the concepts of effective stress combined with Coulomb failure criterion (Sibson, 1985a).

On the one hand, researchers focused on understanding the onset of fault reactivation due to a linear increase in fluid pressure in triaxial loading apparatus. They demonstrated that when the fluid pressure build-up is homogeneous along the fault, the reactivation follows the Coulomb failure criterion (French et al., 2016; Rutter & Hackston, 2017; Scuderi et al., 2017; Ye & Ghassemi, 2018). When the fluid pressure build-up presents a gradient, due to a low permeability fault zone or a large imposed injection rate, the Coulomb failure criterion still holds if considering the average fluid pressure distributed all along the fault. However, the degree of fluid pressure

© 2023. The Authors.

This is an open access article under the terms of the [Creative Commons Attribution License](https://creativecommons.org/licenses/by/4.0/), which permits use, distribution and reproduction in any medium, provided the original work is properly cited.

heterogeneity will influence the onset of fault reactivation (Cebry et al., 2022; Passelègue et al., 2018) and control the dynamics of the induced slip front (Passelègue et al., 2020) as expected theoretically (Garagash & Germanovich, 2012; Sáez et al., 2022). Moreover, injection rate was found to affect the nature of ruptures, with high injection rates triggering dynamic ruptures at a lower fluid pressure and for a smaller nucleation size (Gori et al., 2021), and slow injection rates leading to fault creep (Wang et al., 2020).

At a larger scale of observations, stress heterogeneities related to fast fluid injection or low permeability fault are at the origin of foreshocks and induce swarms signature even at the scale of the laboratory (Cebry & Mclasley, 2021). In addition, *fluid injection* experiments were also conducted at a larger scale along natural faults, allowing to study the influence of elastic stress redistribution due to partial site at the injection site on the induced seismic sequence (De Barros et al., 2016; Guglielmi et al., 2015), and on the fluid pressure front diffusion (Cappa et al., 2018; Frédéric Cappa et al., 2022).

On the other hand, researchers have also studied the influence of mitigation strategies on induced seismicity. By studying the response of experimental faults to cyclic increases in fluid pressure (Chanard et al., 2019; Noël, Passelègue, et al., 2019; Noël, Pimienta, et al., 2019) they have shed light on reactivation mechanisms and the onset of unstable slip. Another mitigation strategy can be related to the use of different fluid properties. Despite that, up to now, few studies focused on the influence of fluids, and their viscosity, on the reactivation and the propagation of the seismic rupture (Bayart et al., 2016; Cornelio et al., 2019; Cornelio & Violay, 2020). The influence of fluid viscosity on earthquake nucleation and propagation is moreover relevant knowing that the fluids naturally flowing into faults can present different viscosities, depending on the presence of gouge and its composition (Brodsky & Kanamori, 2001; Otsuki et al., 1999). Moreover, fluids injected for human activity are also known to span a wide range of viscosity values ranging between ~ 0.1 and 1 mPas for CO_2 storage (Bando et al., 2004), ~ 35 – 500 mPas for wastewater application (Cheryan & Rajagopalan, 1998; M. Lu & Wei, 2011), and $2,200$ mPas for hydraulic fracturing (Esmailirad et al., 2016). It is then critical to understand how fluid viscosity affects the *nucleation and propagation* of earthquakes.

For what concerns earthquakes *nucleation*, that is, a period that describes the initiation of rupture, different models seem to be able to describe this process (for a review refer to Mclasley, 2019). The pre-slip model, the most observed experimentally (Guérin-Marthe et al., 2019; Latour et al., 2013; Mclasley & Lockner, 2014; Ohnaka & Shen, 1999; Okubo & Dieterich, 1984), describes nucleation by a first quasi-static phase (aseismic slip) followed by an acceleration phase and subsequent dynamic propagation, with the nucleation length L_c , the size at which the aseismically slipping patch enters the acceleration phase (Latour et al., 2013). It takes the general form of:

$$L_c = \frac{\mu D_c}{(\sigma_n - P_f) \Delta f} k \quad (1)$$

assuming a linear slip weakening law, with μ the shear modulus of the bulk material, D_c the critical slip distance describing the stress weakening, Δf the friction drop characterizing the event, σ_n and P_f respectively the normal load and the fluid pressure, and k a constant depending on geometry (Uenishi & Rice, 2003). Note that different definitions of L_c are found depending on the theoretical framework in which nucleation is studied; with linear slip-weakening (Andrews, 1976; Uenishi & Rice, 2003) or rate and state friction (Ampuero & Rubin, 2008; Rubin & Ampuero, 2005). An increase in pore pressure induces a reduction in the effective normal stress, which increases the critical length L_c , resulting in a slow, stable fault slip before eventually fast dynamic events. Indeed, recent in situ experimental tests (Guglielmi et al., 2015) and numerical studies (Bhattacharya & Viesca, 2019) suggest that fluid overpressure initially promotes a slow slip. However, little is known about the influence of fluid viscosity on the nucleation length or nucleation process in general (Cornelio & Violay, 2020).

More is known for what concerns the effect of fluid viscosity on the frictional response. The theory of lubrication describes the interface weakening based on the lubrication conditions; boundary lubrication conditions (when the load is exclusively supported by solid contacts), mixed lubrication conditions (when the load is supported by both solid contacts and the fluid), and full lubrication conditions (when a continuous film of fluid supports the totality of the load). One of the first studies to treat this topic was Brodsky and Kanamori (2001). Depending on fault slip and the given characteristic lubrication lengths, the fault weakening can, in specific cases, be described by elastohydrodynamic lubrication. Recent experiments performed on rocks focused on understanding the influence of viscous fluids on faults mechanical behavior, spanning the three aforementioned lubrication conditions

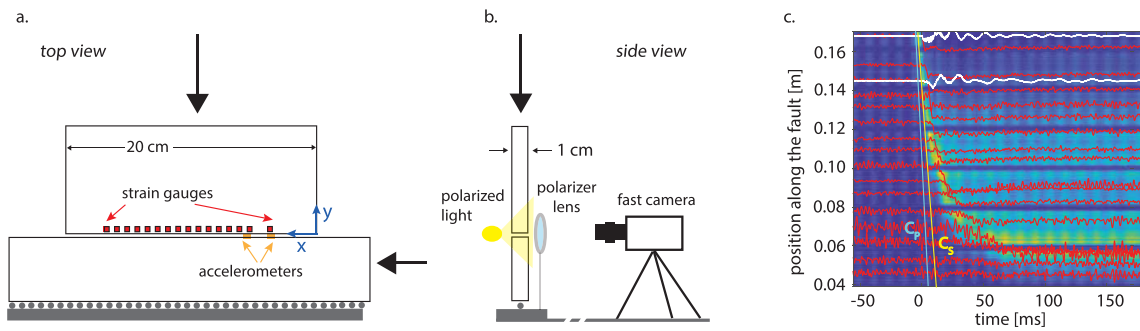


Figure 1. Scheme of the experimental setup where the two polymethyl methacrylate samples are loaded to recreate the artificial fault ((a) top view, (b) side view). The fault is equipped with a strain gauges array at 1.5 mm from the interface and two accelerometers at 5 mm from the fault. A fast camera continuously acquired videograms allowing the tracking of the rupture front. Please note that the drawing is not up to scale (c). Example of a precursor event with synchronization of the different acquisition system: photoelasticity (in colorbar), strain gauges (in red), and accelerometers (in white).

and showing that fluid viscosity influences fault stability (Cornelio et al., 2020) and weakening mechanism (Cornelio et al., 2019, 2020; Cornelio & Violay, 2020). In particular, they showed the dynamic friction to be strictly dependent on fluid viscosity and slip velocity, suggesting, under given conditions, elastohydrodynamics as a possible weakening mechanism (Cornelio et al., 2019). Experimental work performed on analog material (Bayart et al., 2016) studied the influence of lubricant on rupture dynamics, showing that in the case of boundary lubrication conditions some seismic source parameters such as fracture energy and stress drop can be affected by the presence of viscous lubricants. In particular fracture energy values were found significantly larger than for the dry case (\sim one order of magnitude). Moreover, it was shown that the presence of viscous lubricant did not modify the equation of motion expected assuming Linear Elastic Fracture Mechanics (LEFM; Svetlizky et al., 2017).

The objective of this work is to study the influence of viscous lubricant in the nucleation and propagation of spontaneous frictional ruptures, occurring under mixed lubrication conditions, not explored until now.

2. Methods

2.1. Experimental Setup

Spontaneous frictional ruptures were reproduced along artificial interfaces by putting into contact with two polymethyl methacrylate (PMMA) samples in a biaxial apparatus located in the Experimental Rock Mechanics Laboratory in the Swiss Institute of Technologies (Paglialunga et al., 2021; Figures 1a and 1b). Two blocks of dimensions $200 \times 100 \times 10$ mm and $400 \times 100 \times 10$ mm generated an interface of 200×10 mm. The material is characterized by C_P and C_S of respectively of 2,700 and 1,345 m/s. Macroscopic loads were imposed through two hydraulic pumps from Enerpac© applying normal and shear loads. The normal load was kept constant during the whole duration of the experiment while the shear load was applied through a hydraulic manual pump until the fault exhibited instabilities (the loading rate could not be controlled in the current setup). The macroscopic loads were monitored during the experiments using two load cells located between the two pistons and the frames holding the samples. The recording frequency was 100 Hz, acquired through a National Instrument acquisition system.

2.2. Photoelasticity

The nucleation and the propagation of dynamic rupture phenomena were recorded using a high-speed camera Phantom VE0710. The Camera allowed to record images of the complete fault interface with a resolution of $1,280 \times 32$, in fault length and fault width, respectively. The camera is equipped with a dynamic memory buffer for acquisition in trigger mode, allowing to store continuous sequences lasting up to 4 s. The camera was triggered using the accelerometer located close to the interface at location $x = 37$ mm, allowing to record at a sampling rate of 113,000 images/seconds. An exposure time of $1 \mu\text{s}$ was set. The visibility of the fracture propagation was possible thanks to the birefringent properties of PMMA under polarized light, using an LED bar and two polarized filters on each side of the fault (Figure 1b). The interferometric images recorded during nucleation and

rupture propagation allowed us to track the position of the rupture tip during the event. In all the figures showing photoelasticity measurements, the colormap indicates the light contrast with respect to a reference time selected before each event. Strong dynamic stress concentrations will induce a high contrast that will indicate the passage of the rupture front (the colorbar is not showed because it would not add quantitative information).

2.3. Dynamic Strain Gages

To capture the details of dynamic ruptures, the fault was equipped with an array of 16 one-direction (parallel to the fault direction) strain gauges, equally spaced, placed at ~ 1 mm from the interface. Measurements were acquired continuously at a high recording frequency (2 MHz) using a digital oscilloscope. Signals were pre-amplified using Kyowa signal conditioner CDA-900A. This system allows a maximum bandwidth frequency of 500 kHz, allowing the complete capture of the dynamic of the rupture front. Note that strain gauge dimensions prove to be of crucial importance for the analysis of the strain signal. The ones used in this study have a size of 0.2×1.4 mm.

2.4. Accelerometers

In addition to strain gages, two high-frequency accelerometers (type 8309 from Bruel and Kjaer), were glued at different locations along the fault interface, 5 mm away from the fault plane at 62 and 37 mm from the right edge of the fault. They were recording preferentially the acceleration motions in the slip direction. These accelerometers present a flat response up to 54 kHz, within a 10% limit interval. The acceleration signals were monitored through a four channels Nexus conditioner, which converted directly the signal in mV/g. These sensors were located in the near-field source domains and were used to compute the near-field acceleration, velocity, and displacement motions during dynamic rupture propagations.

2.5. Experimental Conditions

Experiments were performed both under dry and lubricated conditions. Different mixtures were created to obtain fluids with different viscosities; 100% water, 40% water and 60% glycerol, 15% water and 85% glycerol, and 99% glycerol, with respective viscosities of 1.0, 10.8, 109, 1,226 mPa·s (Cornelio et al., 2020). Please note that these viscosity values are representative of natural and industrial fluids mentioned earlier. In what follows, fluids will be distinguished by their viscosity value. To recreate lubricated conditions, an equal amount of lubricant was dropped along the interface before putting into contact with the two surfaces before each experiment (i.e., lubricant viscosity). The interface was cleaned after each experiment, removing eventual gouge particles and lubricant (if present). Note that all experiments included a sequence of seismic events, between which there was no control over the fault conditions. However, no observable damage occurred during the cumulative seismic sequences induced, given that the surfaces were initially polished with an optical finish, breaking down gouge production.

3. Experimental Results

In the first data set, the effect of different applied normal loads was studied in dry conditions. In a second data set, the normal load was kept constant among the different experiments, but lubrication conditions were changed. The aforementioned three kinds of measurement (high-frequency strain, on-fault acceleration, photoelasticity) were synchronized and used to study the rupture front nucleation and propagation. The time vectors were synchronized through arrival times of the rupture front at location $x = 0.03$ m where all three measurements are available. Rupture velocity evolution was computed from both the strain gauges array and the photograms. In the first case, the arrival time was detected for each strain gauge location assuming a locally constant rupture velocity computed as $C_f = \Delta x / \Delta t$. A similar procedure was followed to compute C_f from the photograms, with the only difference being that the arrival front was detected at discrete equidistant locations along the fault.

3.1. Mechanical Results

Macroscopic stresses were analyzed to study the influence of load and lubrication conditions during stick-slip events. For experiments performed under dry conditions, the applied normal stress was kept constant with final values of ~ 1.75 MPa (SF34), 2.5 MPa (SF35), and 3.5 MPa (SF36). The shear stress was increased until, once

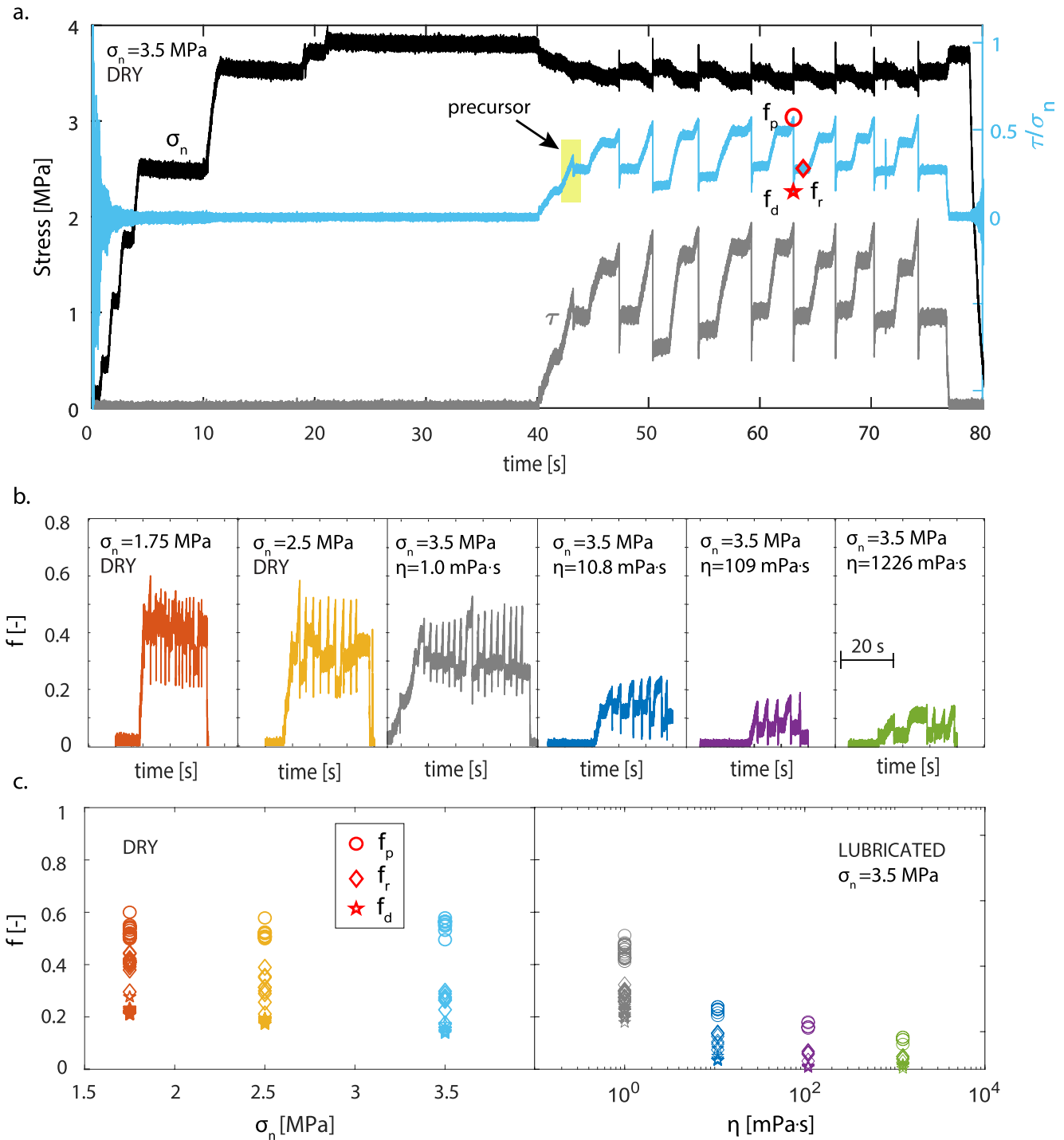


Figure 2. (a) Evolution of macroscopic normal stress (in black), shear stress (in gray), and friction (in cyan) with time for experiment performed in dry conditions at 3.5 MPa normal stress. (b) Evolution of macroscopic friction with time for experiments performed under different conditions. (c) Evolution of peak, residual, and dynamic friction values with normal stress and fluid viscosity. The marker colors refer to the initial normal stress conditions and to the lubrication conditions that is, Red: dry conditions $\sigma_n = 1.75$ MPa; Orange: dry conditions, $\sigma_n = 2.5$ MPa; Cyan: Dry conditions, $\sigma_n = 3.5$ MPa; Gray: $\eta = 1.0$ mPa·s, $\sigma_n = 3.5$ MPa; Blue: $\eta = 10$ mPa·s, $\sigma_n = 3.5$ MPa; Purple: $\eta = 100$ mPa·s, $\sigma_n = 3.5$ MPa; Green: $\eta = 1,200$ mPa·s, $\sigma_n = 3.5$ MPa. This color legend will be kept for all figures unless differently specified.

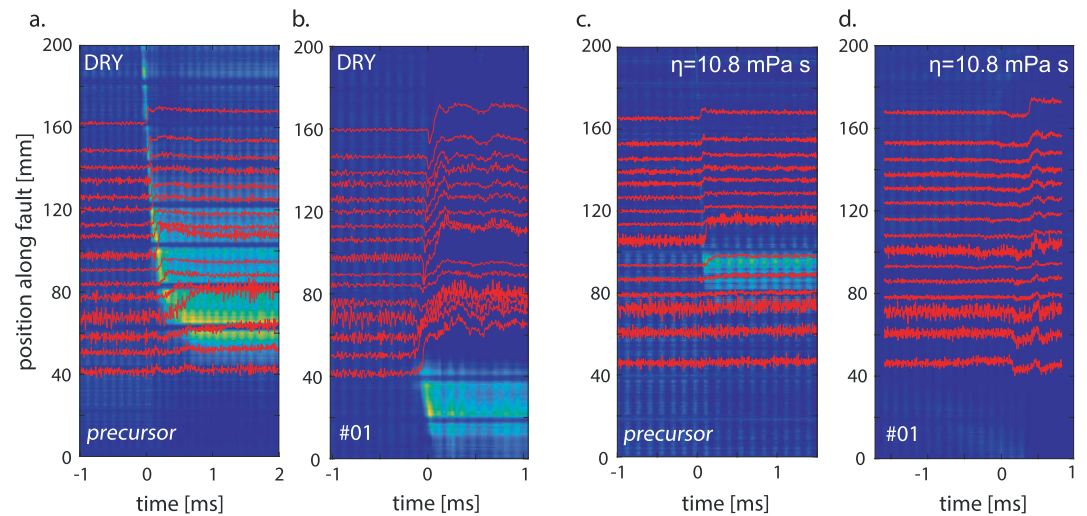


Figure 3. Example of sequence of a precursor event (a, c) and the following main event (b, d) for experiments performed under dry conditions (on the left) and lubricated conditions (on the right). All the precursors nucleated at the fault's edge and, after propagating along a big portion of the fault, they stopped. The main events following them always nucleated in the same portion of the fault where the precursors had previously stopped. Strain evolutions (in red) are showed together with photoelasticity measurements.

reached the fault strength, the emergence of instabilities (i.e., stress drops), characteristic of stick-slip behavior (Figure 2a). The fault strength showed to be consistent for the different tested normal stresses, and stress drops associated with stick-slip events increased slightly with normal stress. For all experiments performed under lubricated conditions, the applied normal stress was ~ 3.5 MPa (the highest normal stress used during dry experiments). However, the different lubrication conditions affected the fault strength (τ_s), which decreased with increasing viscosity. τ_s in dry conditions was found of 1.75 MPa and it decreased to 1.56 MPa in water lubricated ($\eta = 1.0$ mPa \cdot s) conditions. With viscous lubricant τ_s was found of ~ 0.74 MPa for $\eta = 10.8$ mPa \cdot s, 0.56 MPa for $\eta = 109$ mPa \cdot s, and 0.41 MPa for $\eta = 1,226$ mPa \cdot s.

To compare fault stability among the different conditions, the apparent friction (f) was computed as $f = \frac{\tau}{\sigma_n}$ (Figure 2b). Its macroscopic evolution showed the same behavior as the shear stress, exhibiting a peak value (f_p) right before the instability and a drop (Δf) concurrent with the event. The events occurring on the dry interface show the highest friction values ranging between 0.50 and 0.61 for events at 1.75 MPa, 0.50 and 0.58 for events at 2.5 and 3.5 MPa. Much lower peak friction values, in response to lower shear stress, were measured for events occurring under lubricated conditions. In particular, the values ranged between 0.41 and 0.51 for $\eta = 1.0$ mPa \cdot s, 0.20 and 0.24 for $\eta = 10.8$ mPa \cdot s lubricated conditions, 0.16 and 0.18 for $\eta = 109$ mPa \cdot s lubricated conditions, 0.09 and 0.12 for $\eta = 1,226$ mPa \cdot s lubricated conditions.

3.2. Photoelasticity; Precursors, and Main Events

The nucleation stage of instabilities was studied by combining interferometric images provided by the high-speed camera and strain gauges data. High-speed photoelastic measurements of the interface allowed the detection of the rupture front (from nucleation to dynamic propagation) through analysis of stress concentration at the crack tip resulting in a high light contrast on the images (Figures 3 and 4). The rupture front was manually picked for each event and its evolution in time was studied.

As can be observed from the macroscopic shear stress evolution (Figure 2a), the series of mainshocks were preceded by a precursor event. Here we define precursors as the ruptures that did not propagate throughout the whole fault, but rather stopped at a given location, depending on the local stress distribution. Their propagation, even if incomplete, modified the on-fault stress distribution, influencing the activation of the following event. The first main (i.e., complete) event often nucleated in the exact fault location where the precursor had previously stopped (Figure 3), as also observed in Gvirtzman and Fineberg (2021). For example, as the rupture nucleated at the sample's edge, it propagated dynamically through a big part of the interface and slowed down until stopping

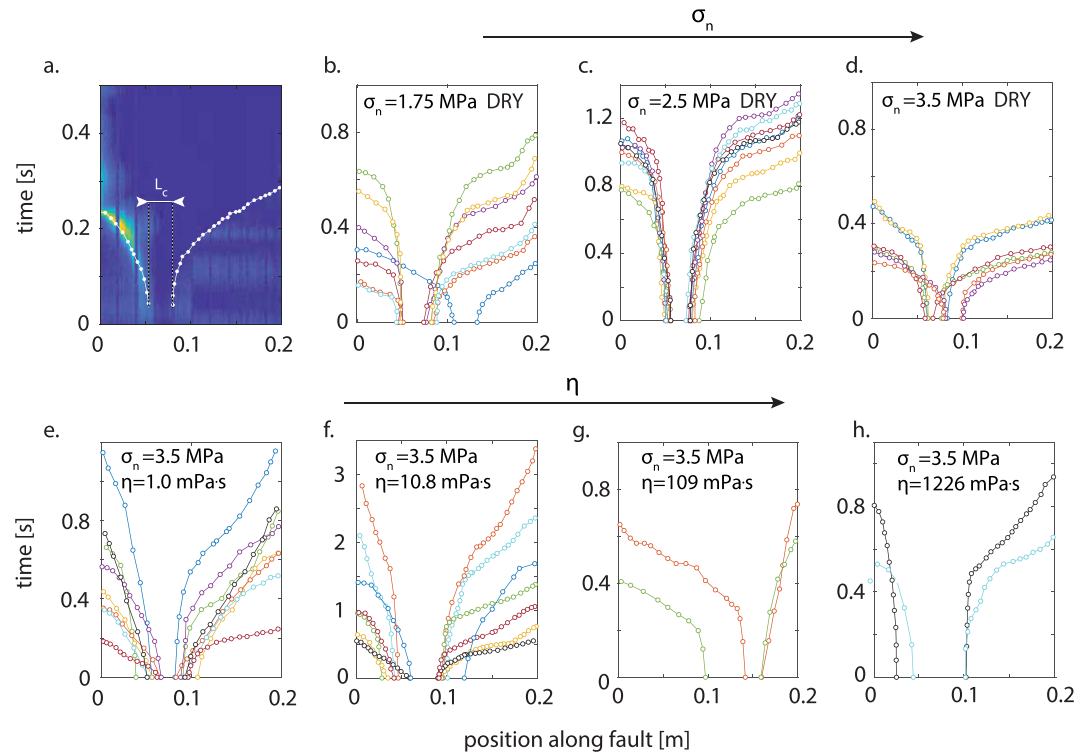


Figure 4. (a) Example of photoelasticity measurements used to track the rupture evolution profiles. The profiles were manually picked (dashed white). All main ruptures nucleated in the central part of the fault and propagated bilaterally. (b–d) events occurring for increasing applied normal stress. (e–h) events occurring for increasing fluid viscosity (under constant normal stress of 3.5 MPa). Colors indicate different events.

at position 37 mm. The following main event (Figure 3b) nucleated at the same location at which the precursor had previously stopped (~ 50 mm), and propagated bilaterally rupturing the whole fault. A similar behavior was observed for the precursor event that occurred in lubricated conditions with $\eta = 10.8$ mPa \cdot s lubricant (Figure 3c). The precursor nucleated at the fault edge, propagated dynamically and stopped at position $x \sim 62$ mm. The next event nucleated exactly at the same location and propagated bilaterally rupturing the whole fault (note that strain perturbation visible after the nucleation front are secondary waves).

3.3. Influence of Lubrication Conditions on the Nucleation of Instability

From now on, we will focus only on the study of mainshocks. Remarkably, all the events that completely ruptured the interface were bilateral (i.e., propagating simultaneously in both directions with respect to their nucleation patch), with nucleation occurring in the central part of the interface. Most of the ruptures showed a symmetric propagation, while a few were affected by the sample's edge effects (Figures 4g and 4h). All the events showed a phase attributable to rupture nucleation, where a quasi-static rupture growth was observed, followed by an acceleration phase and a dynamic propagation phase. The nucleation length measured in this study corresponds to the first slipping patch measurable in time from photoelasticity measurements as depicted in Figure 4a, and might not correspond exactly to the one measured in Latour et al. (2013).

Nevertheless, L_c showed a clear dependence on applied normal load and fault lubrication conditions. In dry conditions, L_c decreased for increasing normal load as expected (Latour et al., 2013), with values of ~ 0.025 – 0.045 m for $\sigma_n = 1.75$ MPa, ~ 0.017 – 0.038 m for $\sigma_n = 2.5$ MPa, and ~ 0.07 – 0.025 m for $\sigma_n = 3.5$ MPa, in agreement with Equation 1. Under lubricated conditions, L_c increased with increasing fluid viscosity, with values of ~ 0.03 – 0.07 m for $\eta = 1.0$ mPa \cdot s, ~ 0.05 – 0.08 m for $\eta = 10$ mPa \cdot s, ~ 0.06 – 0.08 m for $\eta = 100$ mPa \cdot s, ~ 0.055 – 0.085 m for $\eta = 022$ mPa \cdot s (Figure 5).

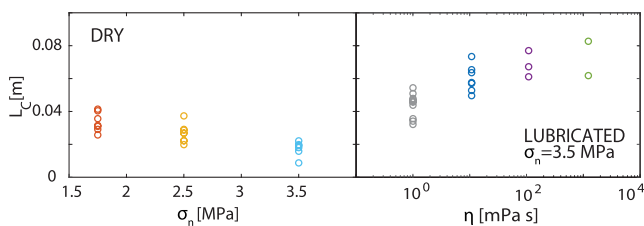


Figure 5. Nucleation length (L_c) evolution with applied normal load (on the left) and fault lubrication conditions (on the right). Color legend refers to the one described in Figure 2.

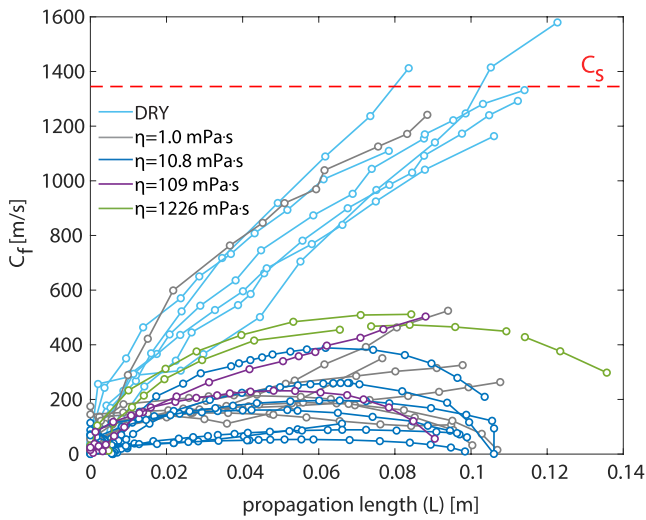


Figure 6. Evolution of the rupture speed with propagation length for all the events under the different lubrication conditions.

3.4. Rupture Propagation Velocity Evolution

Rupture velocity during propagation (only the side approaching the right edge of the fault of the bilateral rupture is considered for this purpose) showed the largest values for events occurring on the dry interface with values ranging between 1,200 and 1,500 m/s (reaching an asymptotic value around C_s , and in some cases exceeding it; Figure 6). Events occurring on the lubricated interface showed lower C_f . In particular, C_f was between 122 and 525 m/s for $\eta = 1.0 \text{ mPa} \cdot \text{s}$, 61 and 332 m/s for $\eta = 10.8 \text{ mPa} \cdot \text{s}$, 120 and 503 m/s for $\eta = 109 \text{ mPa} \cdot \text{s}$, and 449 and 511 m/s for $\eta = 1,226 \text{ mPa} \cdot \text{s}$. It can be observed that conversely to rupture velocity evolutions recorded in dry conditions, in agreement with what the equation of motion would describe, under mixed lubricated conditions ruptures showed an initially stable propagation with slow and intermediate rupture velocity fronts along the interface.

3.5. Estimates of the Energy Release Rate During Propagation

The measurements of the 16 horizontal strain gauges array gave insights about, besides the evolution of the rupture fronts propagating during the events, the strain evolution during the experiments, and its perturbation at the passage of the rupture front (Figure 7). Events propagating under dry conditions were characterized by notable strain perturbations, which became less and less evident for the events occurring under lubricated conditions. Moreover, from the strain evolutions profiles, it can be observed that the rupture propagation time is comparable to the local strain perturbation time window in the case of dry conditions, while it is larger in the case of lubricated conditions (Figure 7).

To better understand how rupture dynamics were affected by the chosen lubrication conditions, an analysis of the fracture energy released at the passage of the rupture front was adopted. Using theoretical predictions of LEFM, the fracture energy at the rupture tip could be inverted for selected stick-slip events, assuming the propagating front as a shear rupture (Svetlizky & Fineberg, 2014). Stress perturbations occurring at the passage of the rupture tip can be described by LEFM as follows:

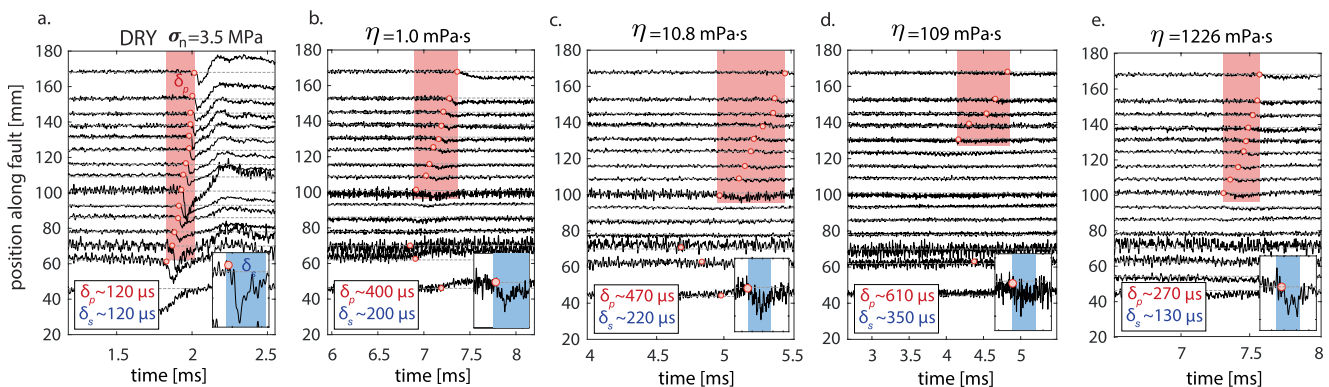


Figure 7. Strain evolution with time during rupture nucleation for events occurring under different conditions; dry at 3.5 MPa (a), $\eta = 1.0$ (b), $\eta = 10.8$ (c), $\eta = 109$ (d), $\eta = 1,226$ (e). The insets show a zoom-in of ϵ_{xx} perturbation caused by the passage of the rupture front. Red markers indicate rupture's arrival time at each measuring location. The red shaded area indicates rupture propagation time window and the blue shaded area indicates strain perturbation time window.

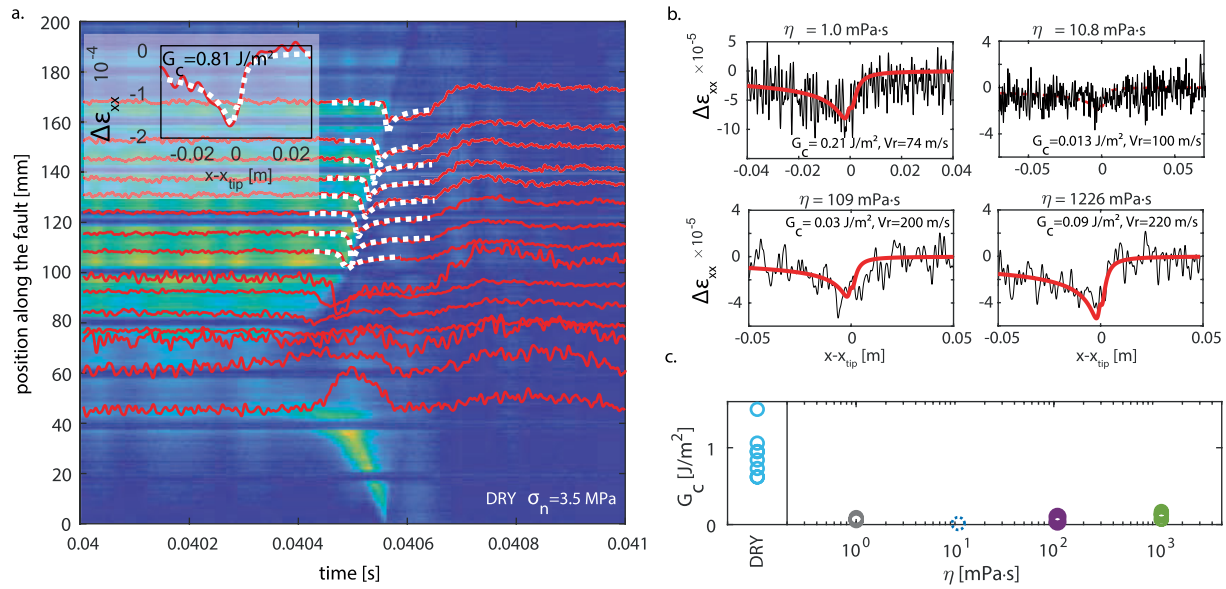


Figure 8. Estimates of fracture energy under dry and mixed lubrication conditions. (a) Event 01 in dry conditions at 3.5 MPa normal stress. Strain evolutions are synchronized with photoelasticity measurements (in the background). In dashed white the theoretical predictions expected from Linear Elastic Fracture Mechanics (LEFM) for the portion of the fault along which the rupture propagated dynamically. The inset shows the fit of the strain perturbation with LEFM, resulting in an estimated $G_c = 0.81 \text{ J/m}^2$. (b) Examples of fit of strain perturbation predicted by LEFM with the measured ones for lubricated conditions. (c) Estimated values of G_c for the different tested conditions. (Color legend refers to the one described in Figure 2.)

$$\Delta\sigma_{xy}(\theta, r, C_f) = \frac{K_{II}(C_f)}{\sqrt{2\pi r}} \Sigma_{xy}^{II}(\theta, C_f) \quad (2)$$

where θ, r are polar coordinates with origin at the crack tip, $K_{II}(C_f)$ is the stress intensity factor and $\Sigma_{xy}^{II}(\theta, C_f)$ is the angular variation. The stress intensity factor $K_{II}(C_f)$ can be related to the fracture energy by imposing an energy balance which equates fracture energy (G_c) to the energy release rate (G) through the following:

$$G = G_c = \frac{(1 - \nu^2)}{E} K_{II}^2(C_f) f_{II}(C_f) \quad (3)$$

where $f_{II}(C_f) = \frac{\alpha_s}{(1-\nu)D(C_f)} \frac{C_f^2}{C_s^2}$, and α_s and $D(C_f)$ are functions of the rupture velocity.

Since the system is initially loaded (macroscopic loads), the stress (and strain) distribution at the crack tip is influenced by initial stresses (σ_{xx}, σ_{yy}) and residual stress (τ) and the respective singular contributions of the stress field. For this reason, to obtain the strain variations ($\Delta\epsilon_{xx}$), the initial strain (acting before the event) was subtracted from ϵ_{xx} .

The fracture energy estimated for the dry interface ranged between 0.62 and 1.5 J/m^2 , values in agreement with the literature for similar experimental conditions (Bayart et al., 2016; Svetlizky & Fineberg, 2014). Under lubricated conditions the estimated fracture energy was significantly lower, ranging between 0.05 and 0.09 J/m^2 for $\eta = 1.0 \text{ mPa} \cdot \text{s}$, $\sim 0.01 \text{ J/m}^2$ for $\eta = 10.8 \text{ mPa} \cdot \text{s}$, between 0.04 and 0.05 J/m^2 for $\eta = 109 \text{ mPa} \cdot \text{s}$ and between 0.07 and 0.17 J/m^2 for $\eta = 1,226 \text{ mPa} \cdot \text{s}$ (Figure 8). An evident trend shows that under mixed lubrication conditions the fracture energy characterizing the main rupture front is lower than for dry conditions.

3.6. Radiations During Rupture Propagation

The recorded on-fault accelerations were compared for the different experiments. It is important to keep in mind that the accelerometer used to record the data is placed at $x = 62 \text{ mm}$, a location at which the ruptures have already transitioned into their dynamic propagation phase (for all conditions except for $\eta = 109 \text{ mPa} \cdot \text{s}$ lubricated case for which the rupture nucleated around $x = 50 \text{ mm}$ (Figure 4g); the accelerometer placed at $x = 37 \text{ mm}$

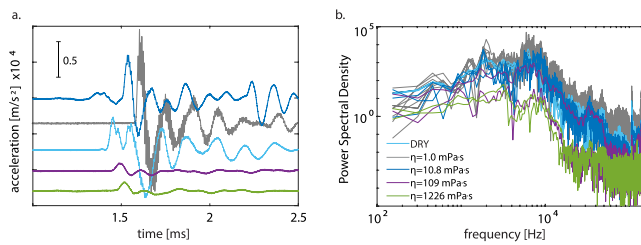


Figure 9. Acceleration data (a) and respective Power Spectral Density (b) for events occurring under different lubrication conditions.

was used instead). Different acceleration contents can be noticed among the different conditions (Figure 9). The accelerations measured for events in water-lubricated conditions show the highest amplitude, followed by the ones measured for events in dry conditions. The acceleration amplitude progressively decreases with increasing lubricant viscosity, reaching the lowest for events under $\eta = 1,226 \text{ mPa} \cdot \text{s}$ lubricated conditions.

This data was then used to compute the acceleration Power Density Spectrum. Lubrication influenced the radiation content. The power density (proportional to the moment magnitude) of events occurring on the dry interface and water-lubricated is the highest and slightly decreases for higher viscosity mixture-lubricated interfaces. The lowest amplitude (i.e., lowest expected moment magnitude) is observed for $\eta = 1,226 \text{ mPa} \cdot \text{s}$ lubricated interface.

In this spectrum the main peak is common to all the experimental conditions, corresponding to a given corner frequency value (f_c). This frequency is about $\sim 6.5 \text{ kHz}$, most probably related to the rupture velocity and the length of dynamic propagation. Considering a rupture velocity of $\sim 500 \text{ m/s}$ (average rupture velocity measured for dry conditions), and dividing by the corner frequency $\sim 6.5 \text{ kHz}$, a characteristic length of $\sim 0.08 \text{ m}$ is obtained, comparable to the propagation length measured through photoelasticity during dynamic propagation. However, such corner frequency suggests that only a small patch of the fault propagates dynamically in presence of viscous fluids. Assuming a rupture speed of 100 m/s (as the ones measured for lubricated conditions), the expected propagation length is $\sim 1.5 \text{ cm}$, which appears to be smaller than the propagation length expected from photoelasticity (i.e., $L \sim 6\text{--}8 \text{ cm}$).

Slip rate ($V(t) = 2 \int a dt$) and coseismic slip ($D(t) = \int V dt$) were computed through integration in time of the acceleration signal. The rise time (t_r), time characterizing the local slip duration, was chosen by looking at the slip evolution. The time window started at the time at which $D(t) \neq 0$, and ended at t_r , time at which $D(t)$ reached a plateau. The successive decreasing evolution of slip is not characteristic of the main rupture but of reflections traveling along the interface, which can be neglected in what follows. It should be noted that accelerometers are only installed on one side of the fault (top sample), as such, the slip measured is representative of only half of the total fault slip. This assumes slip symmetry, which should be guaranteed since the two samples are made of the same material, they have comparable dimensions, and they share the same thickness. The $V(t)$ and $D(t)$ evolutions were computed for the different lubrication conditions, and notable differences were observed between them (Figure 10). V_{max} values increased with increasing normal stress and decreased under lubricated conditions, decreasing with increasing viscosity, reaching the lowest values for $\eta = 1,226 \text{ mPa} \cdot \text{s}$ ($\sim 0.08\text{--}0.16 \text{ m/s}$). A similar trend was observed for the coseismic slip. The highest final slip values were measured for the dry interface at high normal stress ($\sim 85\text{--}110 \mu\text{m}$), while they decreased, for the lubricated interface, with increasing lubricant viscosity.

4. Discussion

Our experimental results show that in dry conditions, increasing the normal stress acting on the fault leads to a decrease in the nucleation length, while the frictional strength of the interface remains roughly constant. These results are compatible with previous studies (Guérin-Marthe et al., 2019; Harbord et al., 2017; Latour et al., 2013). In lubricated conditions, our experiments highlight that increasing the fluid viscosity along the fault leads to (a) a decrease in the peak strength of the fault, and of the subsequent stress drop during instabilities, (b) an increase in the nucleation length for constant normal stress, (c) a decrease in the rupture velocity and fracture energy along the interface, and (d) a decrease in the size of the events in terms of slip and radiations.

4.1. Finite Ruptures Precede Main Ruptures Series

The conducted experiments systematically showed a first precursor event, followed by a series of main (i.e., complete) ones. The arrest of a rupture can occur for different reasons such as prestress distribution (Ke et al., 2018), interface rheology (Rubino et al., 2022), locally increased toughness (Gvirtzman & Fineberg, 2021), fault geometry (Sibson, 1985b). In the present experiments, we believe that rupture arrest was mostly controlled

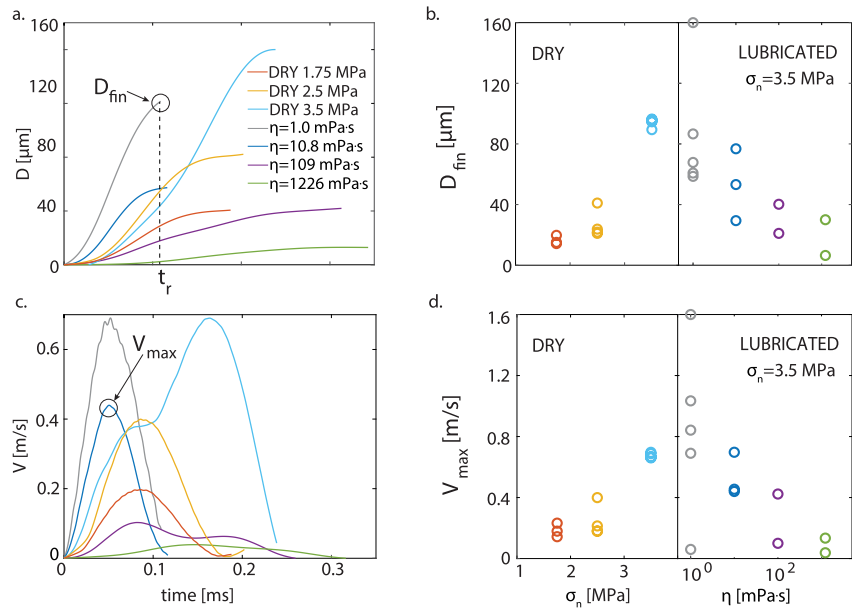


Figure 10. (a) Example of displacement evolution with time for the different lubrication conditions. t_r indicates the local raise time. (b) Final displacement (D_{fin}) for increasing applied normal load (on the left) and increasing fluid viscosity (on the right). (c) Example of slip velocity evolution with time for the different lubrication conditions. (d) Maximum slip velocity (V_{max}) for increasing applied normal load (on the left) and increasing fluid viscosity (on the right). (Color legend refers to the one described in Figure 2.)

by the pre-stress distribution controlled by the experimental boundary conditions. The finite size of our samples, together with the position of the stopper (which prevents the top sample from sliding together with the bottom one), controls the initial stress distribution along the fault, resulting heterogeneous. For this reason, after the first event propagates for a portion of the fault, it will probably stop at the first encountered stress heterogeneity. This will modify the stress distribution, easing the propagation of the subsequent event. For example, in Rubino et al. (2022) the rupture arrest is explained by the velocity strengthening behavior of the gouge layer that acts as a barrier. In our experiments, the barrier is rather represented by an initial stress heterogeneity caused by the imposed boundary conditions.

4.2. Influence of Fluid Viscosity on the Reactivation of the Fault

A clear evolution of macroscopic friction with applied normal stress and lubrication conditions was observed in these experiments. The events occurring on the dry interface show the highest friction values, which decreased, in lubricated conditions, for increasing fluid viscosity.

Under dry conditions, friction is defined as $f = \frac{A_{contact}}{A_{apparent}} \frac{\tau_y}{\sigma_n}$, with $A_{contact}$ the real contact area, $A_{apparent}$ the nominal contact area and τ_y the solid shear strength and σ_n the macroscopic normal load (for a review on the adhesion theory of friction please refer to Scholz, 2019, ch.2). The increase in normal load is reflected in an increase in the area of contact, leading to a constant friction value.

However, the presence of a fluid film between the two surfaces (i.e., lubricated conditions) can interfere with the load distribution. Depending on the thickness of the film (controlled by loading condition, surface roughness, and fluid properties), the different conditions can be: boundary lubrication, mixed lubrication, or full lubrication. Please note that in this context such definitions are used to describe initial contact conditions and could slightly differ from the ones used in the lubrication theory which assume a sliding velocity. These experiments show a significant reduction in peak friction for lubricated conditions, indicating that the boundary lubrication condition should be excluded as a plausible option. In fact, under boundary lubrication conditions the stress acting on the interface is by definition supported completely by the solid contacts. For this reason, the peak friction is expected to be similar to the one of the dry interface. The dynamic friction value will be the one mostly affected by the presence of a lubricant film, showing a significant reduction (Cornelio et al., 2019; Gori et al., 2021).

We assumed the fault to be subjected to mixed lubrication conditions, meaning that the applied normal load is born partly by the *solid contacts* and partly by the *lubricated contacts*. The fluid will occupy part of the initial contact area, reducing the solid contacts, hence drastically decreasing the peak friction. Moreover, this effect will be more accentuated for higher viscosity values, due to the higher resistance to motion generating higher lubrication pressures and a larger area of lubricated contacts. This well reflects what was observed with macroscopic stress evolution (Figure 2), that is, the large decrease in static fault strength in presence of highly viscous fluids, allowing to induce rupture events at much lower stress conditions than in the dry case.

4.3. Influence of Fluid Viscosity on Nucleation Length

As seen in the introduction, the nucleation length can, in case of homogeneous faults, be described by the following equation assuming the slip-weakening law (Ida, 1972): $L_c = \frac{\mu D_c}{\sigma_n \Delta f}$. Under the same assumption, this equation can be rewritten as $L_c \propto \frac{\mu G_c}{(\sigma_n \Delta f)^2}$.

We can therefore speculate on which quantities affect the observed evolution of L_c , by considering Δf as the macroscopic measured friction drops, and G_c the values of fracture energy inverted through strain gauges measurements. Starting by the latter, we observed G_c values drastically reduced under lubrication conditions, and slightly increased for increasing lubricant viscosity. At the same time, the friction drop was found to decrease for increasing lubricant viscosity. Considering that σ_n was kept constant for all the performed experiments and equal to 3.5 MPa, we can then assert that the observed behavior of L_c mainly depends, in the case of mixed lubrication conditions, on the competition between the change in G_c and the change in friction drop for the different viscosities.

Furthermore, as shown in the *Results* section, we estimated for lubricated conditions lower fracture energy (G_c) driving the main rupture front. This is different from what was measured under boundary lubrication conditions (Bayart et al., 2016, 2018) which shows fracture energy increasing with the presence of a lubricant. Considering a linear slip weakening law, the fracture energy is expected to be proportional to the critical slip distance (D_c). Hence, in light of Equation 1, we would expect higher G_c values for larger nucleation lengths. However, this is true only in the case of comparable initial stress (as occurs in boundary lubrication conditions). As it was highlighted through the macroscopic stress evolution (Figure 2), the performed events occurred under mixed lubrication conditions; the static shear stress (and peak friction) dramatically decreased, with an associated much lower stress (and friction) drop. In the slip-weakening framework, a lower peak stress with an associated lower stress drop generates a smaller fracture energy. All is finally controlled by a competition between the change in D_c and the change in $\Delta \tau$ for the different experimental conditions. This explains why in our events the expected scaling $G_c \propto L_c$ is not observed.

4.4. Lubrication Affects the Rupture Mode (Crack-Like Versus Pulse-Like)

It is known that the characteristic time during which the event occurs carries important information about the nature of the event itself. The rise time, intended as the local slip duration, was computed considering the slip evolution integrated from the on-fault accelerations as described in Section 3.5 (Figure 11a, inset). On the other side, another characteristic time was computed; the source duration T_d , intended as the total expected rupture duration (time that the rupture spends to travel along the interface [Figure 11a]). It was computed as an average between the maximum expected source duration computed as $T_{d,max} = L/C_f$ with L the propagation length and C_f the measured rupture speed, and the lower bound $T_{d,min}$, measured as the time the rupture took to propagate from the accelerometer position to the fault edge. The comparison of these two characteristic times (t_d) gave insights into the mode of rupture; crack-like versus pulse-like. It is known (X. Lu et al., 2007) that for

- $t_r \approx T_d$ the rupture will show a crack-like behavior (ruptures for which the interface keeps sliding in the wake of the crack tip)
- $t_r \ll T_d$ the rupture will show a pulse-like behavior (ruptures for which the interface heals in the wake of the crack tip and relocks).

We observed that for the events occurring under dry conditions the two characteristic times are comparable $t_r \approx T_d$, an indicator of crack-like ruptures. However, this is not the case for the events occurring under lubricated

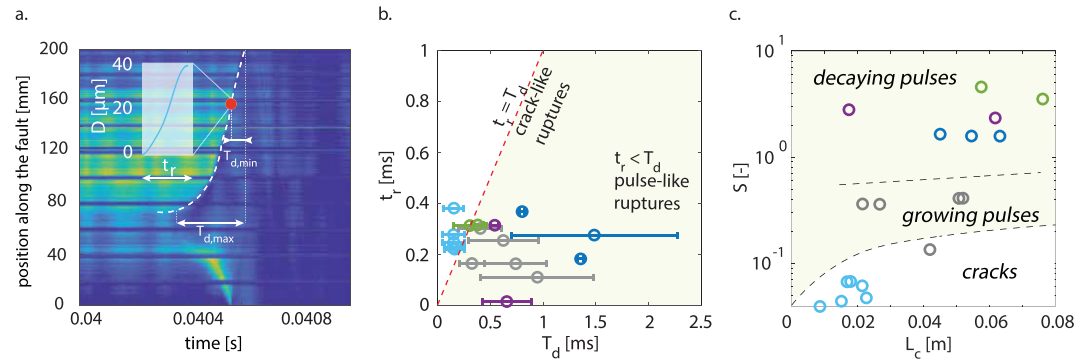


Figure 11. (a) Example of how the rise time (t_r) and the source duration (T_d) would seem in one of the observed events. (b) Comparison of t_r values with T_d values for the different events. The slope 1:1 indicates ruptures propagating in a crack-like manner, while the area for which $t_r < T_d$ indicates ruptures propagating in a pulse-like manner. (c) Dependence of the different rupture modes on seismic ratio S and nucleation length L_c (inspired by Figure 5 in Gabriel et al., 2012). For low S values crack-like ruptures are observed, for increasing S values the rupture modes transition into growing pulses and for even higher S values to decaying pulses. Note that the dashed curves are drawn by hand to differentiate the different observed regimes and do not follow any analytical or numerical solution. (Color legend refers to the one described in Figure 2.)

conditions. Regardless of the fluid viscosity, the rise time was always found much smaller compared to the source duration $t_r \ll T_d$, an indicator of pulse-like ruptures (Figure 1b).

Moreover, we know that the stress state and nucleation length can control the rupture mode (Gabriel et al., 2012). The seismic ratio was then computed for the different events as $S = \frac{f_s - f_0}{f_0 - f_d}$, with f_s and f_d respectively the static and dynamic friction and f_0 the initial friction value measured for each event. The values of friction were chosen respectively as: $f_s = 0.6$ (maximum static friction measured in the present experiments for dry interface) and $f_d = 0$ (minimum dynamic friction that can be reached). The evolution of S values with nucleation length (L_c) seems in agreement with the literature (Gabriel et al., 2012), showing; for low S values and small L_c values emergence of crack-like ruptures, for higher S values and larger L_c values emergence of pulse-like ruptures (Figure 11c). The latter can be partitioned further into growing pulses and decaying pulses. This discrimination is possible by observing the rupture velocity evolution profiles. As aforementioned, the velocity evolution of the events occurring with water as lubricant show a first overall steady behavior suggesting *fault plane healing* (Freund, 1979), followed by an acceleration toward the fault edge, a signature of growing pulses. The opposite happens for the velocity evolution of the events occurring with viscous mixtures as lubricant; after an overall steady behavior, the rupture slows down toward the fault edge, a signature of decaying pulses.

The emergence of pulse-like ruptures can also be observed in Figure 8 where for such conditions, after the strain perturbation concurrent with the passage of the rupture front, strain promptly returns to the static value, suggesting healing of the interface behind the crack tip. While for events occurring under dry conditions, the strain rather reaches a residual value, suggesting continuous sliding. As suggested by observing the dependence of the rupture mode on the seismic ratio, the cause for the observed pulse-like ruptures could be the low prestress characterizing these events. Theoretical work (Zheng & Rice, 1998), and more recently experimental work (X. Lu et al., 2007) already showed how for low prestress values, and in velocity weakening conditions, the rupture preferentially propagates as self-healing rather than as a crack. Indeed, for events under lubricated conditions, we observed a dramatic reduction of shear strength with respect to the case under dry conditions. This implies a much lower prestress level that could facilitate pulse-like over crack-like ruptures. Moreover, laboratory experiments on granite (McLaskey et al., 2015) showed that such slip pulses could emerge either at free sample edges or right outside of the nucleation patch, as it happens in our observed events.

4.5. Radiation

The radiation analyzed through the acceleration data was revealed to be influenced by the lubrication conditions. The overall radiation was maximum in the dry and water-lubricated cases. It decreased slightly for the $\eta = 10.8 \text{ mPa} \cdot \text{s}$ lubricated case and kept decreasing for higher fluid viscosities. This can be explained by different, but probably connected, phenomena such as; (a) viscous damping, (b) lubrication mechanism, and (c) reduced stress drop.

Viscous damping commonly occurs when thin viscous fluid films are constrained between surfaces. The fluid lubricating the interface damps the acceleration waves traveling through it, resulting in a lower radiated content. Figure 9 shows clear evidence of dissipation for high-viscosity lubricant fluids. By comparing the values of maximum slip rate V_{\max} with values of maximum rupture velocity $C_{f,\max}$ for different lubrication conditions, one can observe that for a similar range of $C_{f,\max}$, V_{\max} is lower for increasing lubricant viscosity, an indicator of higher damping and/or dissipation.

Slightly different is the lubrication mechanism involving the lubrication pressure P_{lub} caused by fault motions. Such lubrication pressure increase would reduce the contact area, resulting in reduced high-frequency radiation expected from asperity breakage. This has also been observed during the 1999 Chi-Chi earthquake in Taiwan (Ma et al., 2003), where the gouge layer in the fault was considered to behave as a viscous material. They observed in one portion of the fault a reduction in high-frequency energy, probably due to high displacement and velocity which allowed the increase of lubrication pressure, and reduced the contact asperities.

The presence of lubricants led to a reduction of fault frictional strength, with repercussions on the magnitude of the experienced stress drops (significantly reduced with respect to dry conditions). A smaller stress drop will inevitably generate a lower radiated content, as observed in these experiments. Given that all the events occurred under lubricated conditions (manifesting a lower stress drop) were associated with a pulse-like behavior, one might draw the conclusion that pulse-like ruptures generate a lower radiated content, opposite to what showed by Lambert et al. (2021; larger radiated energy for pulse-like ruptures). However, the two results can be actually consistent with each other. In our study, the lower radiation is only related to the difference in magnitude of the stress drops characterizing pulse-like and crack-like ruptures, while Lambert et al. (2021) compared ruptures of the same stress drop.

5. Conclusion and Implications for Natural Earthquakes

Our experimental results show that the presence of a lubricant along faults could promote low-stress regions due to a strong reduction of the peak friction coefficient, enhancing the emergence of pulse-like ruptures propagating at low or intermediate seismic velocities. If the on-fault conditions are such that the lubrication responds to a mixed lubrication regime (surface roughness, fluid viscosity, and applied load), then the conclusions drawn in this study could suggest some of the possible causes that make some earthquakes not grow *fast* (at the Rayleigh wave speed) and *big* (i.e., with high radiated energy), but rather propagate *slow* (at portions of the *S* wave speed) and *small* (i.e., smaller radiation content). The presence of a viscous layer can, under the aforementioned conditions, drastically reduce the fault strength, implying, as intuitively as it seems, an easier fault reactivation. However, despite this, given the small stress drop that accompanies it, the rupture would be slower and radiate less. Moreover, these ruptures would initiate in larger nucleation regions, implying a larger portion of the fault slipping aseismically before it starts to propagate dynamically. This could describe the local emergence of slow ruptures or pulse-like phenomena in low-stress areas which are not expected to be explained by high fluid pressure, for instance in clay-rich environments.

Data Availability Statement

The raw data of the performed experiments can be found at the following address:
<http://doi.org/10.5281/zenodo.7560665>.

References

- Ampuero, J. P., & Rubin, A. M. (2008). Earthquake nucleation on rate and state faults—Aging and slip laws. *Journal of Geophysical Research*, *113*(B1), 1–21. <https://doi.org/10.1029/2007JB005082>
- Andrews, D. J. (1976). Rupture velocity of plane strain shear cracks. *Journal of Geophysical Research*, *81*(32), 5679–5687. <https://doi.org/10.1029/JB081i032p05679>
- Bando, S., Takemura, F., Nishio, M., Hihara, E., & Akai, M. (2004). Viscosity of Aqueous NaCl solutions with dissolved CO₂ at (30–60) °C and (10–20) MPa. *Journal of Chemical & Engineering Data*, *49*, (5), 1328–1332. <https://doi.org/10.1021/jc049940f>
- Bayart, E., Svetlizky, I., & Fineberg, J. (2016). Slippery but tough: The rapid fracture of lubricated frictional interfaces. *Physical Review Letters*, *194*301(116), 1–5. <https://doi.org/10.1103/PhysRevLett.116.194301>
- Bayart, E., Svetlizky, I., & Fineberg, J. (2018). Rupture dynamics of heterogeneous frictional interfaces. *Journal of Geophysical Research: Solid Earth*, *123*(5), 3828–3848. <https://doi.org/10.1002/2018JB015509>
- Bhattacharya, P., & Viesca, R. (2019). Fluid-induced aseismic fault slip outpaces pore-fluid migration. *Science*, *364*(6439), 464–468. <https://doi.org/10.1126/science.aaw7354>

Acknowledgments

This project was partially funded by a grant of the program TelluS-ALEAS of CNRS-INSU (project “DRHEX”). F.P. and M.V. acknowledge support by the European Research Council Starting Grant project 757290-BEFINE. F.P. thanks Chiara Cornelio for support in the choice and realization of the lubricant mixtures. The authors thank Alexandre Schubnel for the use of the accelerometers. The authors thank Chun-Yu Ke and an anonymous reviewer, as well as the associated editor and editor, for their constructive comments which improved the manuscript. Open access funding provided by Ecole Polytechnique Federale de Lausanne.

- Brodsky, E., & Kanamori, H. (2001). Elastohydrodynamic lubrication of faults. *Journal of Geophysical Research: Solid Earth*, 106(B8), 16357–16374. <https://doi.org/10.1029/2001jb000430>
- Cappa, F., Guglielmi, Y., Nussbaum, C., & Birkholzer, J. (2018). On the relationship between fault permeability increases, induced stress perturbation, and the growth of aseismic slip during fluid injection. *Geophysical Research Letters*, 45(20), 11012–11020. <https://doi.org/10.1029/2018GL080233>
- Cappa, F., Guglielmi, Y., Nussbaum, C., De Barros, L., & Birkholzer, J. (2022). Fluid migration in low-permeability faults driven by decoupling of fault slip and opening. *Nature Geoscience*, 15(9), 747–751. <https://doi.org/10.1038/s41561-022-00993-4>
- Cebry, S. B. L., Ke, C. Y., & McLaskey, G. C. (2022). The role of background stress state in fluid-induced aseismic slip and dynamic rupture on a 3 m laboratory fault. *Journal of Geophysical Research: Solid Earth*, 127(8), 1–19. <https://doi.org/10.1029/2022JB024371>
- Cebry, S. B. L., & McLaskey, G. (2021). Seismic swarms produced by rapid fluid injection into a low permeability laboratory fault. *Earth and Planetary Science Letters*, 557, 116726. <https://doi.org/10.1016/j.epsl.2020.116726>
- Chanard, K., Nicolas, A., Hatano, T., Petrelis, F., Latour, S., Vinciguerra, S., & Schubnel, A. (2019). Sensitivity of acoustic emission triggering to small pore pressure cycling perturbations during brittle creep. *Geophysical Research Letters*, 46(13), 7414–7423. <https://doi.org/10.1029/2019GL082093>
- Cheryan, M., & Rajagopalan, N. (1998). Membrane processing of oily streams. Wastewater treatment and waste reduction. *Journal of Membrane Science*, 151(1), 13–28. [https://doi.org/10.1016/S0376-7388\(98\)00190-2](https://doi.org/10.1016/S0376-7388(98)00190-2)
- Cornelio, C., Passelègue, F. X., Spagnuolo, E., Di Toro, G., & Violay, M. (2020). Effect of fluid viscosity on fault reactivation and coseismic weakening. *Journal of Geophysical Research: Solid Earth*, 125(1), e2019JB018883. <https://doi.org/10.1029/2019JB018883>
- Cornelio, C., Spagnuolo, E., Di Toro, G., Nielsen, S., & Violay, M. (2019). Mechanical behavior of fluid-lubricated faults. *Nature Communications*, 10(1), 1–7. <https://doi.org/10.1038/s41467-019-09293-9>
- Cornelio, C., & Violay, M. (2020). Effect of fluid viscosity on earthquake nucleation. *Geophysical Research Letters*, 47(12), 1–9. <https://doi.org/10.1029/2020GL087854>
- De Barros, L., Daniel, G., Guglielmi, Y., Rivet, D., Caron, H., Payre, X., et al. (2016). Fault structure, stress, or pressure control of the seismicity in shale? Insights from a controlled experiment of fluid-induced fault reactivation. *Journal of Geophysical Research: Solid Earth*, 121(6), 4506–4522. <https://doi.org/10.1002/2015JB012633>. Received
- Ellsworth, W. L. (2013). Injection-induced earthquakes. *Science*, 341, 1–8. <https://doi.org/10.1126/science.1225942>
- Esmailirad, N., White, S., Terry, C., Prior, A., & Carlson, K. (2016). Influence of inorganic ions in recycled produced water on gel-based hydraulic fracturing fluid viscosity. *Journal of Petroleum Science and Engineering*, 139, 104–111. <https://doi.org/10.1016/j.petrol.2015.12.021>
- French, M. E., Zhu, W., & Banker, J. (2016). Fault slip controlled by stress path and fluid pressurization rate. *Geophysical Research Letters*, 43(9), 4330–4339. <https://doi.org/10.1002/2016GL068893>
- Freund, L. B. (1979). The mechanics of dynamic shear crack propagation. *Journal of Geophysical Research: Solid Earth*, 84(B5), 2199–2209. <https://doi.org/10.1029/JB084iB05p02199>
- Gabriel, A., Ampuero, J. P., Dalguer, L. A., & Mai, P. M. (2012). The transition of dynamic rupture styles in elastic media under velocity-weakening friction. *Journal of Geophysical Research*, 117(B9). <https://doi.org/10.1029/2012JB009468>
- Garagash, D. I., & Germanovich, L. N. (2012). Nucleation and arrest of dynamic slip on a pressurized fault. *Journal of Geophysical Research: Solid Earth*, 117(10), 1–27. <https://doi.org/10.1029/2012JB009209>
- Gori, M., Rubino, V., Rosakis, A. J., & Lapusta, N. (2021). Dynamic rupture initiation and propagation in a fluid-injection laboratory setup with diagnostics across multiple temporal scales. *Proceedings of the National Academy of Sciences of the United States of America*, 118(51). <https://doi.org/10.1073/pnas.2023433118>
- Guérin-Marthe, S., Nielsen, S., Bird, R., Giani, S., & Di Toro, G. (2019). Earthquake nucleation size: Evidence of loading rate dependence in laboratory faults. *Journal of Geophysical Research: Solid Earth*, 124(1), 689–708. <https://doi.org/10.1029/2018JB016803>
- Guglielmi, Y., Cappa, F., Avouac, J. P., Henry, P., & Elsworth, D. (2015). Seismicity triggered by fluid injection—Induced aseismic slip. *Science*, 348(6240), 1224–1226. <https://doi.org/10.1126/science.aab0476>
- Gvirtzman, S., & Fineberg, J. (2021). Nucleation fronts ignite the interface rupture that initiates frictional motion. *Nature Physics*, 17(9), 1037–1042. <https://doi.org/10.1038/s41567-021-01299-9>
- Harbord, C. W. A., Nielsen, S., De Paola, N., & Holdsworth, R. (2017). Earthquake nucleation on rough faults. *Geology*, 45(10), 931–934. <https://doi.org/10.1130/G39181.1>
- Ida, Y. (1972). Cohesive force across the tip of a longitudinal-shear crack and Griffith's specific surface energy. *Journal of Geophysical Research*, 77(20), 3796–3805. <https://doi.org/10.1029/jb077i020p03796>
- Ke, C. Y., McLaskey, G. C., & Kammer, D. S. (2018). Rupture termination in laboratory-generated earthquakes. *Geophysical Research Letters*, 45(23), 12784–12792. <https://doi.org/10.1029/2018GL080492>
- Lambert, V., Lapusta, N., & Perry, S. (2021). Propagation of large earthquakes as self-healing pulses or mild cracks. *Nature*, 591, 252–258. <https://doi.org/10.1038/s41586-021-03248-1>
- Latour, S., Schubnel, A., Nielsen, S., Madariaga, R., & Vinciguerra, S. (2013). Characterization of nucleation during laboratory earthquakes. *Geophysical Research Letters*, 40(19), 5064–5069. <https://doi.org/10.1002/grl.50974>
- Leclère, H., & Fabbri, O. (2013). A new three-dimensional method of fault reactivation analysis τ . *Journal of Structural Geology*, 48, 153–161. <https://doi.org/10.1016/j.jsg.2012.11.004>
- Lu, M., & Wei, X. (2011). Bioresource Technology Treatment of oilfield wastewater containing polymer by the batch activated sludge reactor combined with a zerovalent iron/EDTA/air system. *Bioresource Technology*, 102(3), 2555–2562. <https://doi.org/10.1016/j.biortech.2010.11.103>
- Lu, X., Lapusta, N., & Rosakis, A. (2007). Pulse-like and crack-like ruptures in experiments mimicking crustal earthquakes. *Proceedings of the National Academy of Sciences of the United States of America*, 104(48), 18931–18936. <https://doi.org/10.1073/pnas.0704268104>
- Ma, K. F., Brodsky, E. E., Mori, J., Ji, C., Song Teh-Ru, T. R. A., & Kanamori, H. (2003). Evidence for fault lubrication during the 1999 Chi-Chi, Taiwan, earthquake (Mw7.6). *Geophysical Research Letters*, 30(5), 3–6. <https://doi.org/10.1029/2002gl015380>
- Majer, E., Baria, R., Stark, M., Oates, S., Bommer, J., Smith, B., & Asanuma, H. (2007). Induced seismicity associated with enhanced geothermal systems. *Geothermics*, 36(3), 185–222. <https://doi.org/10.1016/j.geothermics.2007.03.003>
- McLaskey, G. (2019). Earthquake initiation from laboratory observations and implications for foreshocks. *Journal of Geophysical Research: Solid Earth*, 124(12), 882–904. <https://doi.org/10.1029/2019JB018363>
- McLaskey, G., Kilgore, B., & Beeler, N. (2015). Slip-pulse rupture behavior on a 2 m granite fault. *Geophysical Research Letters*, 42(17), 7039–7045. <https://doi.org/10.1002/2015GL065207>
- McLaskey, G., & Lockner, D. (2014). Preslip and cascade processes initiating laboratory stick slip. *Journal of Geophysical Research*, 119(8), 6323–6336. <https://doi.org/10.1002/2014JB011220>

- Noël, C., Passelègue, F., Giorgetti, C., & Violay, M. (2019). Fault reactivation during fluid pressure oscillations: Transition from stable to unstable slip. *Journal of Geophysical Research: Solid Earth*, *124*(11), 940–953. <https://doi.org/10.1029/2019JB018517>
- Noël, C., Pimienta, L., & Violay, M. (2019). Time-dependent deformations of sandstone during pore fluid pressure oscillations: Implications for natural and induced seismicity. *Journal of Geophysical Research: Solid Earth*, *124*(1), 801–821. <https://doi.org/10.1029/2018JB016546>
- Ohnaka, M., & Shen, L. (1999). Scaling of the shear rupture process from nucleation to dynamic propagation: Implications of geometric irregularity of the rupturing surfaces. *Journal of Geophysical Research*, *104*(B1), 817–844. <https://doi.org/10.1029/1998JB900007>
- Okubo, P., & Dieterich, J. (1984). Effects of physical fault properties on frictional instabilities produced on simulated faults. *Journal of Geophysical Research: Solid Earth*, *89*(B7), 5817–5827. <https://doi.org/10.1029/JB089iB07p05817>
- Otsuki, Y., Kajiwaru, T., & Funatsu, K. (1999). Numerical simulations of annular extrudate swell using various types of viscoelastic models. *Polymer Engineering and Science*, *39*(10), 1969–1981. <https://doi.org/10.1002/pen.11590>
- Paglialunga, F., Passelègue, F., Brantut, N., Barras, F., Lebihain, M., & Violay, M. (2021). On the scale dependence in the dynamics of frictional rupture: Constant fracture energy versus size-dependent breakdown work (pp. 1–35). Retrieved from <http://arxiv.org/abs/2104.15103>
- Passelègue, F. X., Almakari, M., Dublanchet, P., Barras, F., Fortin, J., & Violay, M. (2020). Initial effective stress controls the nature of earthquakes. *Nature Communications*, *11*(1), 1–8. <https://doi.org/10.1038/s41467-020-18937-0>
- Passelègue, F. X., Brantut, N., & Mitchell, T. (2018). Fault reactivation by fluid injection: Controls from stress state and injection rate. *Geophysical Research Letters*, *45*(23), 12837–12846. <https://doi.org/10.1029/2018GL080470>
- Rubin, A. M., & Ampuero, J. P. (2005). Earthquake nucleation on (aging) rate and state faults. *Journal of Geophysical Research*, *110*(2), 1–24. <https://doi.org/10.1029/2005JB003686>
- Rubino, V., Lapusta, N., & Rosakis, A. J. (2022). Intermittent lab earthquakes in dynamically weakening fault gouge. *Nature*, *606*(7916), 922–929. <https://doi.org/10.1038/s41586-022-04749-3>
- Rutter, E., & Hackston, A. (2017). On the effective stress law for rock-on-rock frictional sliding, and fault slip triggered by means of fluid injection. *Philosophical Transactions of the Royal Society A: Mathematical, Physical & Engineering Sciences*, *375*(2103), 20160001. <https://doi.org/10.1098/rsta.2016.0001>
- Sáez, A., Lecampion, B., Bhattacharya, P., & Viesca, R. C. (2022). Three-dimensional fluid-driven stable frictional ruptures. *Journal of the Mechanics and Physics of Solids*, *160*, 104754. <https://doi.org/10.1016/j.jmps.2021.104754>
- Scholz, C. H. (2019). *The mechanics of earthquakes and faulting*. Cambridge University Press.
- Scuderi, M. M., Collettini, C., & Marone, C. (2017). Frictional stability and earthquake triggering during fluid pressure stimulation of an experimental fault. *Earth and Planetary Science Letters*, *477*, 84–96. <https://doi.org/10.1016/j.epsl.2017.08.009>
- Sibson, R. H. (1985a). A note on fault reactivation. *Journal of Structural Geology*, *7*(6), 751–754. [https://doi.org/10.1016/0191-8141\(85\)90150-6](https://doi.org/10.1016/0191-8141(85)90150-6)
- Sibson, R. H. (1985b). Stopping of earthquake rupture at dilational jogs. *Nature*, *316*, 6–9.
- Svetlizky, I., & Fineberg, J. (2014). Classical shear cracks drive the onset of dry frictional motion. *Nature*, *509*(7499), 205–208. <https://doi.org/10.1038/nature13202>
- Svetlizky, I., Kammer, D., Bayart, E., Cohen, G., & Fineberg, J. (2017). Brittle fracture theory predicts the equation of motion of frictional rupture fronts. *Physical Review Letters*, *118*(12), 125501. <https://doi.org/10.1103/PhysRevLett.118.125501>
- Uenishi, K., & Rice, J. R. (2003). Universal nucleation length for slip-weakening rupture instability under nonuniform fault loading. *Journal of Geophysical Research*, *108*(B1). <https://doi.org/10.1029/2001JB001681>
- Wang, L., Kwiatek, G., Rybacki, E., Bonnelye, A., Bohnhoff, M., & Dresen, G. (2020). Laboratory study on fluid-induced fault slip behavior: The role of fluid pressurization rate. *Geophysical Research Letters*, *47*(6), 1–12. <https://doi.org/10.1029/2019GL086627>
- Ye, Z., & Ghassemi, A. (2018). Injection-induced shear slip and permeability enhancement in granite fractures. *Journal of Geophysical Research: Solid Earth*, *123*(10), 9009–9032. <https://doi.org/10.1029/2018JB016045>
- Zheng, G., & Rice, J. R. (1998). Conditions under which velocity-weakening friction allows a self-healing versus a cracklike mode of rupture. *Bulletin of the Seismological Society of America*, *88*(6), 1466–1483. <https://doi.org/10.1785/BSSA0880061466>